Rock Mechanics and Rock Engineering
https://doi.org/10.1007/s00603-021-02655-0

ORIGINAL PAPER

Influence of Temperature and Crystal Orientation on Compressive Strength of Rock Salt Using a Newly Developed High-Pressure Thermal Cell

Amirsalar Moslehy[1] · **Khalid A. Alshibli**[1] · **Timothy J. Truster**[1]

Received: 25 January 2021 / Accepted: 19 September 2021
© The Author(s), under exclusive licence to Springer-Verlag GmbH Austria, part of Springer Nature 2021

Abstract
Rock salt is found in nature either in a single crystal or polycrystalline form, where crystal structure, grain, and grain boundary properties have major effects on its strength. The compressive strength of single-crystal rock salt is highly dependent on the loading direction with respect to rock salt's crystal orientation. Most salt formations are either located in a hot environment or exposed to elevated temperatures. Therefore, the influence of temperature should be considered when evaluating the constitutive behavior of rock salt. In this paper, the details of the design of a new high-pressure thermal cell that can withstand a confining pressure up to 15 MPa and a maximum temperature of 150 °C are presented. Three types of polycrystalline rock salt specimens with different grain and grain boundary properties were synthesized to study the effects of grain and grain boundary properties on the strength properties of polycrystalline rock salt. The results of the experiments were then used to examine the influences of grain size, grain boundary properties, annealing process, and temperature on the unconfined compressive strength of polycrystalline rock salt. In addition, 18 natural single-crystal rock salt specimens were prepared and tested at three different crystal orientations relative to loading direction at different temperatures. Specimens tested parallel to [1 0 0] and 19° to (1 0 0) in (0 1 0) showed quite a similar behavior. However, specimens tested on 30° to (1 0 0) in (0 1 0) exhibited a much higher unconfined compressive strength at 20 °C, while their unconfined compressive strength was significantly reduced when the temperature was increased.

Keywords Single-crystal rock salt · Polycrystalline halite · Unconfined compression · High-temperature · Crystal structure

Abbreviations

ASME	American Society of Mechanical Engineers
BPVC	Boilers and pressure vessels
LVDT	Linear variational differential transformer
PTFE	Polytetrafluoroethylene
PXRD	Powder X-ray diffraction
FCC	Face-centered-cubic
LXRD	Laue X-ray diffraction
ASTM	American Society for Testing and Materials
ε_1	Axial strain
σ_1	Axial stress
σ_u	Unconfined compressive strength
RSS	Resolved shear stress
CRSS	Critical resolved shear stress
RNS	Resolved normal stress
CRNS	Critical resolved normal stress
σ	Applied stress
m	Slip system's Schmid factor
$\varnothing$	Angle between the cleavage or slip plane and σ
λ	Angle between the slip direction and σ

1 Introduction

Salt domes usually trap oil, gas, and valuable minerals beneath them due to their low porosity and impermeability. Extracting trapped resources requires drilling through thousands of meters of rock salt formations which introduces many challenges, such as stability of the wellbore, case collapses, and thermal stresses (Fredrich et al. 2003; Hansen and Leigh 2011). On the other hand, rock salt's low porosity, impermeability, high ductility, and self-healing make salt domes excellent and reliable repositories for hazardous wastes, including nuclear waste, and energy resources

✉ Amirsalar Moslehy
amoslehy@vols.utk.edu

[1] Department of Civil and Environmental Engineering, University of Tennessee, Knoxville, TN 37996, USA

Published online: 04 October 2021

(Marques et al. 2013). Some of the stored hazardous wastes within salt domes are either hot when they are transferred to the domes (such as hot oil or oil drilling operations waste) or may produce heat over time, while they are stored inside the domes (nuclear waste for example) (Davis et al. 1978; Hansen and Leigh 2011). Therefore, the applications of salt domes in the energy industry have initiated studies on the effects of temperature on the behavior of rock salt. Different testing procedures such as triaxial, uniaxial, and creep experiments have been used to investigate temperature's short-term and long-term effects on rock salt (Carter and Hansen 1983; Ter Heege et al. 2005; Lebensohn et al. 2003; Liang et al. 2006; Senseny et al. 1992).

Sedimentary rock salt formations develop as a result of the evaporation of enclosed water bodies, such as lakes; therefore, because of their formation process, they are mostly polycrystalline, bedded, and may include impurities (Xing et al. 2015). They usually retain a very low water content in the range of 0.01–1.00% (De Las Cuevas and Pueyo 1995). Polycrystalline rock salt known as halite is made of a large number of smaller halite crystals (grains) bonded to each other at grain boundaries. Grain boundaries are crystallographically defective regions, where two or more crystals with different crystal orientations bond to each other (Locke et al. 2012). The crystal formation process, whether in the laboratory or in nature, influences the properties of a polycrystalline medium's grains and grain boundaries. The properties of a polycrystalline material's grains such as their size, shape, and crystal perfectness degree affect its strength and behavior (Knudsen 1959; Ostapenko et al. 1993). The grain boundaries and their properties also influence the material's behavior and strength, because they can hinder the movement of crystal dislocations (Mouritz 2012). On the other hand, an elevated ambient temperature normally decreases the strength of polycrystalline materials and increases their ductility (Evans et al. 1970; Takasugi and Izumi 1985). Lebensohn et al. (2003) found increasing the temperature from 20 to 100 °C reduces the compressive strength of polycrystalline halite from 60 to 34 MPa under the same confining pressure of 50 MPa without a noticeable increase in the axial strain and ductility of the material. Ter Heege et al. (2005) reported a decrease in the compressive strength of polycrystalline halite when the material was exposed to elevated temperatures. No obvious changes in the ductility of polycrystalline halite were reported in Ter Heege et al.'s study (2005). The results of the aforementioned studies did not report a significant increase of ductility at elevated temperatures in polycrystalline rock salt's behavior.

Some rock salt formations consist of relatively large halite grains (> 100 mm) that have grown in size during a geological time scale under high tectonic hydraulic pressures (Wawersik and Hannum 1980). At a microscopic scale, the constitutive properties of rock salt are governed by the behavior of rock salt single crystals (grains). The constitutive behavior of rock salt single crystals is anisotropic and their strength can vary based on what crystal orientation they are loaded on. Carter and Heard (1970) tested synthetic melt-grown rock salt single crystals in tension loaded on three different crystal orientations at various temperatures and strain rates. The selected crystal orientations were parallel to [0 0 1], 30° to (1 0 0) in (0 − 1 1), and 45° to [0 0 1] in (0 1 0). The specimens extended on 30° to (1 0 0) in (0 − 1 1) and 45° to [0 0 1] in (0 1 0) were found to have a higher work-hardening rate and higher ultimate tensile strengths, because the secondary slip systems became the dominant slip systems compared top which have higher Critical resolved shear stress (CRSS) values. Moreover, all specimens showed a decrease in the strain-hardening rate and ultimate tensile strength with the increase of temperature and decrease of the applied strain rate. Although the studies conducted on synthetic single-crystal rock salt can be a good starting point in understanding the anisotropic response of rock salt single crystals, the constitutive behavior of natural single-crystal rock salt is not necessarily the same as synthetic rock salt. Natural rock salt single crystals often possess more crystal defects when compared to synthetic rock salt crystals (Sedlmayr 2014). Therefore, natural single-crystal rock salt can fail in an entirely different mode than synthetic rock salt, which is yet not thoroughly studied.

This paper presents the design details of a new thermal cell suitable for testing rocks at elevated temperatures and high confining pressures and compares the compressive strength and ductility of differently prepared polycrystalline rock salt specimens. Each of the prepared polycrystalline rock salt specimens represents a distinct polycrystalline rock salt formation. We then investigate the influence of temperature on ductility and compressive strength of different polycrystalline rock salt specimens. In addition, the effects of crystal orientation and temperature on the behavior of natural single-crystal rock salt are studied by preparing specimens with different crystal orientations and testing them in unconfined compression experiments at various temperatures.

2 High-Pressure Thermal Cell

2.1 Background

The combination of a high confining pressure and an elevated temperature makes designing a thermal cell challenging. Cekerevac et al. (2005) employed a hot bath to circulate hot water inside a coil within a traditional triaxial cell for heating. Cekerevac et al. (2005) cell can withstand a temperature up to 90 °C and a confining pressure up to 2 MPa. Zhang et al. (2010) designed a temperature-controlled

triaxial cell capable of applying thermo-mechanical loading on soft sedimentary rocks. They added a cartridge heater and a temperature sensor inside a conventional triaxial cell controlled by a voltage regulator-based temperature controlling unit able to adjust the temperature at a stable rate. The designed cell's temperature and confining pressure ratings were 90 °C and 10 MPa, respectively. Many high-pressure thermal cells have been designed by modifying either a traditional Bishop triaxial cell (Bishop and Donald 1961) or a Bishop-Wesley triaxial cell (Bishop and Wesley 1975) to add thermal capacities to them (Ghembaza et al. 2015; Uchaipichat et al. 2011). Uchaipichat et al. (2011) added a heater and a temperature sensor inside Bishop-Wesley's triaxial cell to test unsaturated soils. Their modified cell can withstand a temperature up to 60 °C and a confining pressure of 600 kPa. Uchaipichat et al. (2011) decided to employ a glass wall tube instead of a conventional Perspex cylinder after the Perspex cylinder used in their initial design exhibited permanent expansion and chemical reaction during elevated temperature experiments. Ghembaza et al. (2015) adopted Bishop-Wesley triaxial cell as a baseline design to test unsaturated soils using the osmotic method by substituting the conventional Perspex cell cylinder with an aluminum jacket, adding a heating collar outside the cell, and adding a temperature probe inside the cell to make the cell suitable for experiments at a temperature up to 80 °C. MTS Systems Corporation's various thermal triaxial cells as reported in the literature, such as in Mishra and Janecek (2017), are another all-around alternative for rock core testing. Some MTS thermal cells can withstand confining pressures higher than 100 MPa and be operated at temperatures up to 200 °C using external heating bands and cartridge heaters embedded within the lower loading platen. In addition, MTS thermal cells are compatible with MTS chain extensometers for measuring lateral deformations during compression tests. Jaradat and Abdelaziz (2020) developed a modified thermo-mechanical triaxial cell capable of changing the temperature within a range of 0.001–0.4 °C/min for thermo-mechanical loading path tests. The heating source in the thermal cell designed by Jaradat and Abdelaziz (2020) was a thermo-electrical heater installed around the cell chamber. The designed cell can reach a maximum of 70 °C temperature and a maximum of 2 MPa confining pressure.

The choice of the fluid for applying confining pressure and/or transferring the heat to the material being tested significantly impacts the thermal cell's operational temperature. Although water has been used as the heat transfer fluid in the literature (mainly for soil testing purposes), the maximum achievable and safe temperature inside the thermal triaxial cell cannot exceed 90 °C (a safe temperature below water's boiling point). The temperature inside salt domes can reach 150 °C or more due to their depth or the heat produced by the material stored inside the rock salt cavities. Moreover, using water as the confining fluid in the presence of rock salt (in case the membrane separating the specimen and the confining fluid is defective) can lead to specimen dissolution, cell corrosion, and eventually failure of the cell. Therefore, the high-pressure thermal cell designed in this study uses a heat-transfer oil to reach temperatures up to 150 °C and withstand a maximum confining pressure of 15 MPa.

2.2 Base Design

Three common methods are widely used for adding thermal capacities to conventional triaxial cells. Circulation of a fluid within a metallic coil using a hot bath source or a cooling system is the most used design for changing the cell temperature. The coil used in the fluid circulation method is either wrapped around the cell or submerged around the specimen (Alshibli and Jarrar 2020; Cekerevac et al. 2005). In the fluid circulation method, the confining pressure is applied inside the thermal cell using a different fluid. In the second method, a collar heater wrapped around the specimen or the triaxial cell can produce the desired temperature inside the cell (Abdelaziz and Jaradat 2020; Ghembaza et al. 2015). A pressurized fluid applies the confining pressure within the cell similar to the first approach. In the mentioned techniques, if the heating source is mounted outside the cell, the cell chamber needs to transfer the heat to the confining fluid and then the heat is transmitted to the specimen. In the internal heater method (third method), an immersion heater installed inside the cell heats the confining fluid (mostly liquid) to transfer the heat to the specimen (Uchaipichat et al. 2011; Zhang et al. 2010). Based on the heater's wattage and the liquid heat capacity and thermal conductivity of the confining fluid, an internal heater method can increase and equilibrate the temperature much faster than the other two heating methods especially if the cell is not designed for thermal or thermo-mechanical loading paths that may add more challenges. Therefore, the cell designed in this paper employs an internal heater method considering its advantages.

The thermal cell's requirements (holding a maximum confining pressure of 15 MPa and a maximum cell temperature of 150 °C) led to a flange-based design to overcome the applied stresses (Fig. 1). A flange-based cell provides more rigidity and better sealing when compared to a conventional triaxial cell, where the flanges encircle the cell chamber and prevent it from bulging. The increased moment of inertia by adding the flanges to the cell prevents bending at the top and bottom cell plates caused by the internal pressure. In addition, the compressional forces caused by the bolts and nuts attaching the top and bottom plates to the flanges provide enough pressure on the O-ring between the plates and flanges to seal the cell. The new thermal cell is designed according to the American Society of Mechanical Engineers

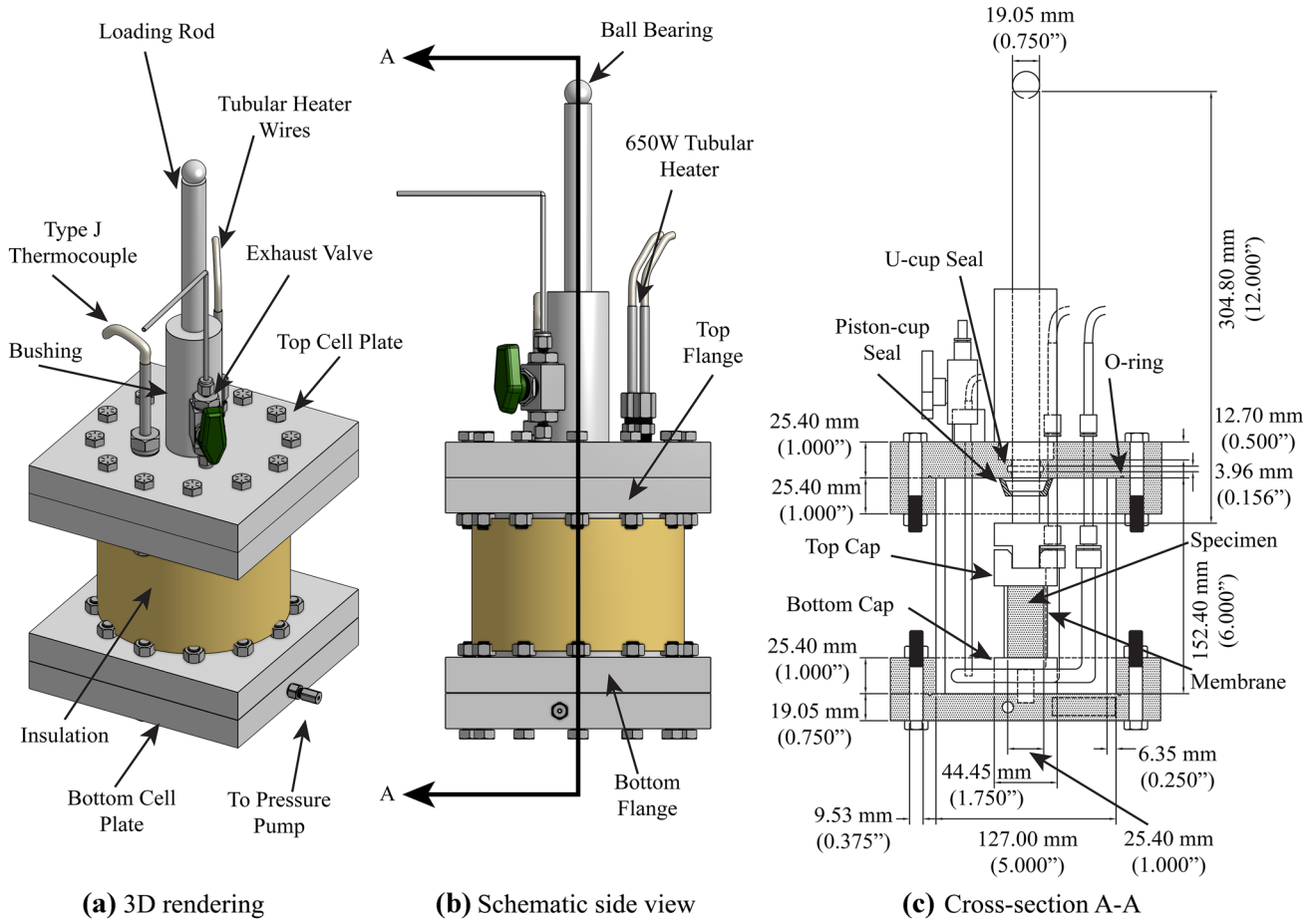

Fig. 1 New high-pressure thermal cell's design

(ASME) Boilers and Pressure Vessels (BPVC) code with a factor of safety of 1.5 applied on the yield stresses of the materials. Figure 2 displays an exploded view of all the components of the new high-pressure thermal cell. 316 stainless steel was selected as the design material for all cell metallic parts to prevent thermal strength losses and corrosion that could potentially happen when testing rock salt. The cell confining chamber has an outer diameter of 127.00 mm (5 in.), a wall thickness of 6.35 mm (0.25 in.), and a height of 152.40 mm (6 in.) to accommodate the heater and other thermal elements within the cell. The 190.50 mm (7.5 in.) long and 25.40 mm (1 in.) thick square flanges were welded to the cell chamber. The top and bottom plates are square with the same dimensions except that their thicknesses are 25.40 mm (1 in.) and 19.05 mm (0.75 in.), respectively. A set of 12 3/8-in. (9.50 mm) fine thread grade 8 bolts and nuts attaches each of the plates to its respective flange. The 19.05 mm (0.75 in.) diameter loading rod can transfer an axial load up to 44.5 kN (10,000 lb) to the material being tested. Figure 3 shows the details of the top plate and the placement of the tying bolts on it.

Figure 4 shows the stainless-steel specimen caps. An O-ring groove was machined on the caps for placing an O-ring around the specimen membrane to secure it. The bottom cap is attached to the cell's bottom plate using a threaded rod to ensure proper alignment of the specimen with the loading rod. Considering the height of the cell chamber and other parts inside the cell, such as specimen caps, the cell can accommodate specimens with heights up to 70 mm (2.75 in.) and diameters up to 35 mm (1.38 in.). Widely used latex membranes have a temperature range of − 55–82 °C; therefore, they cannot be used in experiments at temperatures exceeding 82 °C. Neoprene membranes with a recommended temperature rate of 135 °C are normally the alternative to the latex membranes for hot temperature experiments. However, the pyrolysis of neoprene does not occur before 200 °C (Caballero et al. 2005). Hence, they still can be a viable solution for experiments up to a temperature of 200 °C for an extended time. In addition, a neoprene membrane was placed in a hot bath filled with Therminol 55 heat transfer fluid at a temperature of 150 °C for 60 days before adopting them in this study. No decomposition or

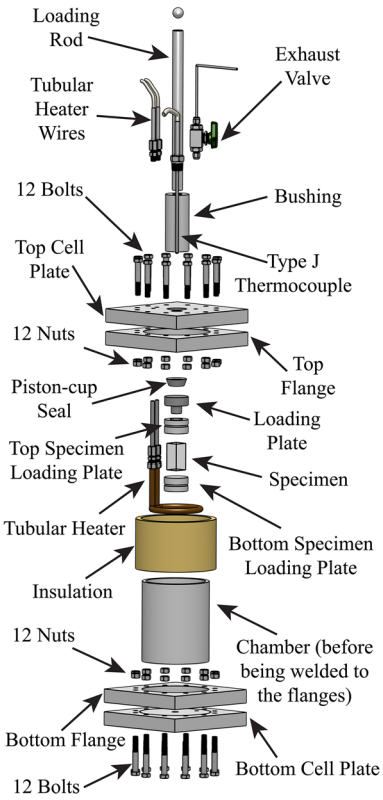

Fig. 2 Exploded view of the high-pressure thermal cell parts

puncture was observed after 60 days. Neoprene membranes have a dimension of $101.60 \times 30.50 \times 0.60$ mm ($4 \times 1.2 \times 0.025$ in.) and can be secured around the specimen and caps using high-temperature silicone O-rings (rated up to 232 °C). Silicone O-rings are dash number 023 size with an outer diameter of 30.25 (1.19 in.), an inner diameter of 26.7 (1.05 in.), and a width of 1.78 mm (0.07 in.). The load frame used in this study was a 44.5 kN (10,000 lb) Sigma-1 servo automated test system manufactured by Geotac coupled with a 44.5 kN (10,000 lb) S-shape load cell by Omega Engineering Inc. The axial deformations in the loading direction are measured using a 76.20 mm (3 in.) range Linear Variational Differential Transformer (LVDT) by Geotac placed on top of the thermal cell. Figure 5 shows a photo of the entire test setup including the load frame and the coupled sensors with it.

2.3 Heating System

The cell's maximum design temperature of 150 °C required a heat transfer fluid with a maximum extended use temperature and a flashpoint above 150 °C that does not emit toxic fumes. A heat transfer fluid with a high thermal conductivity and a low heat capacity also conducts the heat faster and lets the cell temperature become stable much faster. Therminol 55 heat transfer fluid manufactured by Eastman (2020) satisfies all of the four previously mentioned thermal properties and was selected as the heat transfer fluid. Therminol 55's flashpoint is 177 °C with an extended use temperature up to 335 °C. Like the cell designs by Uchaipichat et al. (2011) and Zhang et al. (2010), the initial design in this study used a cartridge heater immersed from the top of the cell. The cartridge heater was 650 W and 152.40 mm (6 in.) long which could heat the fluid in contact with the whole length of the heater. Therminol 55's 0.000961/°C coefficient of thermal expansion causes its density to decrease from 872 kg/m^3 at 20 °C to 784 kg/m^3 at 150 °C. As a result, the heated oil inside the initially designed cell constantly flew towards the cell's top plate, and the cold oil moved to the bottom. The fluid flow inside the cell caused a significant heat gradient of 60 °C between the top plate and the bottom plate when the top plate was at 150 °C. To prevent a heat gradient with the height of the cell, the heat needs to be applied at the bottom of the cell instead of along its height. Installing the heater at the very bottom of the cell causes a density-based fluid circulation which makes the temperature uniform along the height of the cell. However, a straight cartridge heater with enough heat capacity cannot fit in a horizontal direction at the bottom of triaxial cells. Tubular heaters, on the other hand, are bendable; therefore, they can fit inside a thermal triaxial cell. The bendability of the tubular heaters comes at the price of larger diameters and longer cold ends. The tubular heater substituting the initial cartridge heater is an RDN16L1S-27 Watlow heater with a wattage of 650, has a diameter of 9.53 mm (0.375 in.) and a length of 422.28 mm (16.625 in.) and was bent into a ring shape (Fig. 3). The substitution of the heater reduced the heat gradient along the height of the cell to a maximum of 1.7 °C at any time.

The heat controlling unit consists of a Watlow Series CV temperature controlling unit (model CV-CBJHD) and a 152.40 mm (6 in.) long type J thermocouple submerged inside the cell through the top plate. The heating system keeps the cell's temperature within a range of $\pm$ 1.7 °C of the target temperature. A fiberglass insulation jacket is also wrapped around the cell chamber to minimize heat loss. Finally, two continuous temperature-indicating labels with a temperature range of 90–120 °C are attached to the top plate the bottom plates for safety purposes. If for any unforeseen reason the thermocouple fails, these temperature-indicating labels alert the user by changing their color.

2.4 Pressure System

The cell's independent pressure system uses a Teledyne Isco 500D syringe pump with a fluid capacity of 500 ml, and is capable of providing a maximum pressure of 25.85 MPa (3750 psi), and uses the same Therminol 55 heat transfer fluid to apply the confining pressure within

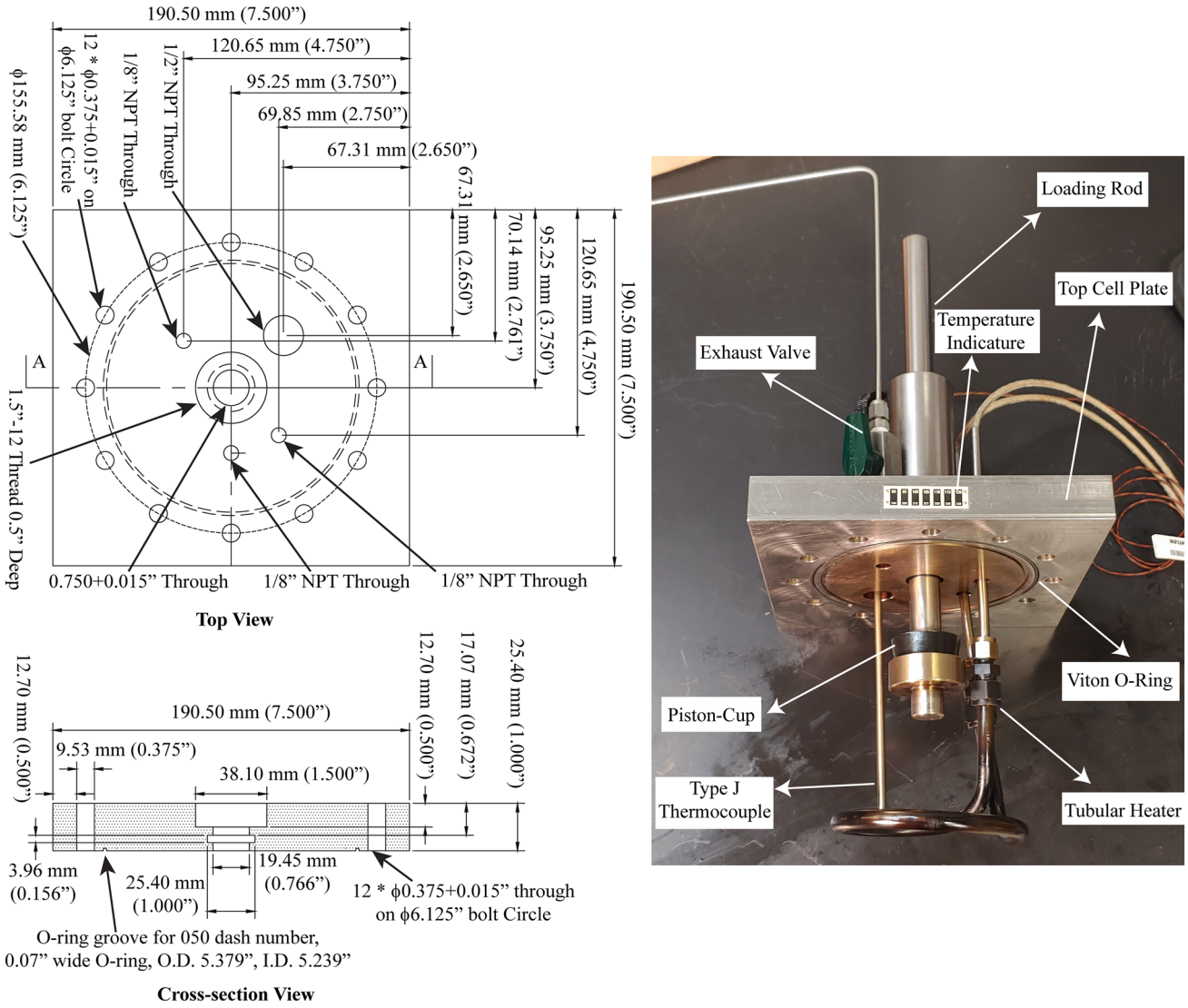

(a) Top plate's top and cross-section view

(b) Top plate's picture

Fig. 3 Thermal cell's top plate and the heating components attached to it

the cell. All the tubes connecting the pump system to the cell are made of 316 stainless steel due to high pressures. An SS-2P4T4 Swagelok valve rated up to 6.9 MPa (1000 psi) at 204 °C or 20.7 MPa (3000 psi) at room temperature is mounted on top of the thermal cell to purge the gas out of the cell at the time of filling it with the heat transfer fluid through the bottom port. The high confining pressure at elevated temperatures makes sealing the cell another challenging task. Viton O-rings rated up to 204 °C seal the gaps between the flanges attached to the top and bottom plates (Fig. 1). Furthermore, a torque of 50 N-m (37 lbs-ft) is applied to the bolts and nuts holding the top and bottom plates to provide enough compression pressure for sealing the mentioned surfaces. Initially, an O-ring loaded rubber U-cup with a rating of 34.5 MPa (5000 psi) and 150 °C was used for sealing the gap between the loading rod and the top plate (Fig. 3). However, during the thermal cell's proof test at a temperature of 150 °C the rubber made U-cup dried after approximately 50 h and caused a fluid leakage around the loading rod. Therefore, a custom-made Viton O-ring loaded U-cup seal rated up to 204 °C with a dimension of 25.40 × 19.05 × 4.75 mm (1 × 0.75 × 0.187 in.) was used instead of the rubber U-cup. The proof tests on the thermal cell after the installation of the custom-made U-cup seal showed it can seal the loading rod at a confining pressure up to 6.9 MPa (1000 psi) at 150 °C, which is the maximum confining pressure the authors intend to use the cell for. However, if a user chooses, a special-made Polytetrafluoroethylene (PTFE) spring-loaded

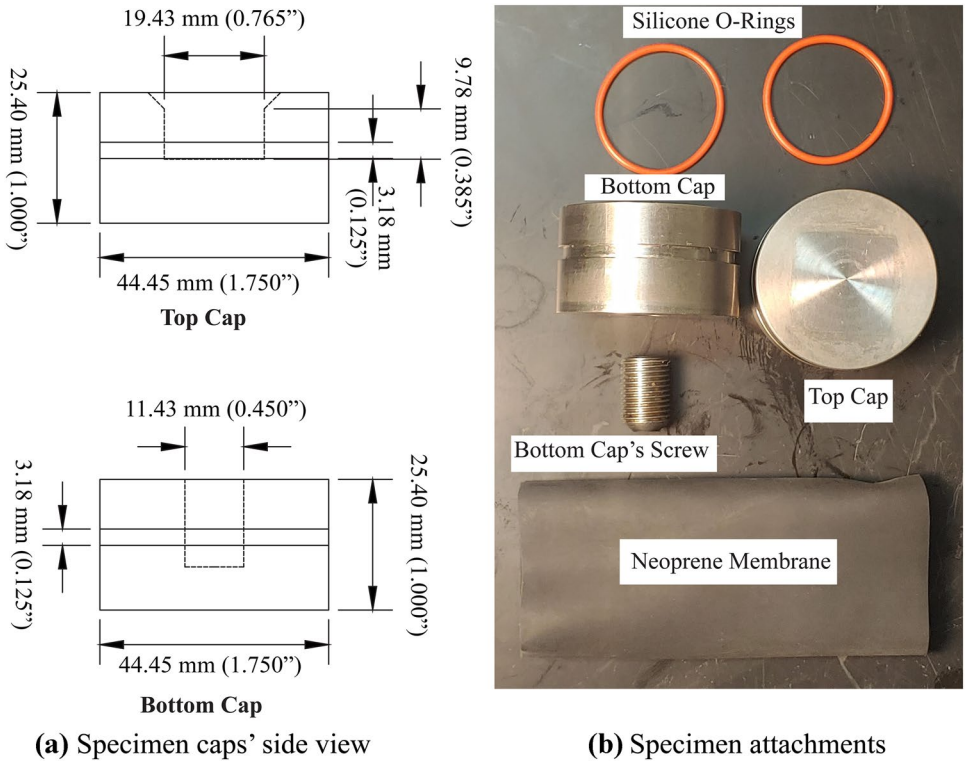

Fig. 4 Specimen end caps, membrane, and silicone O-rings

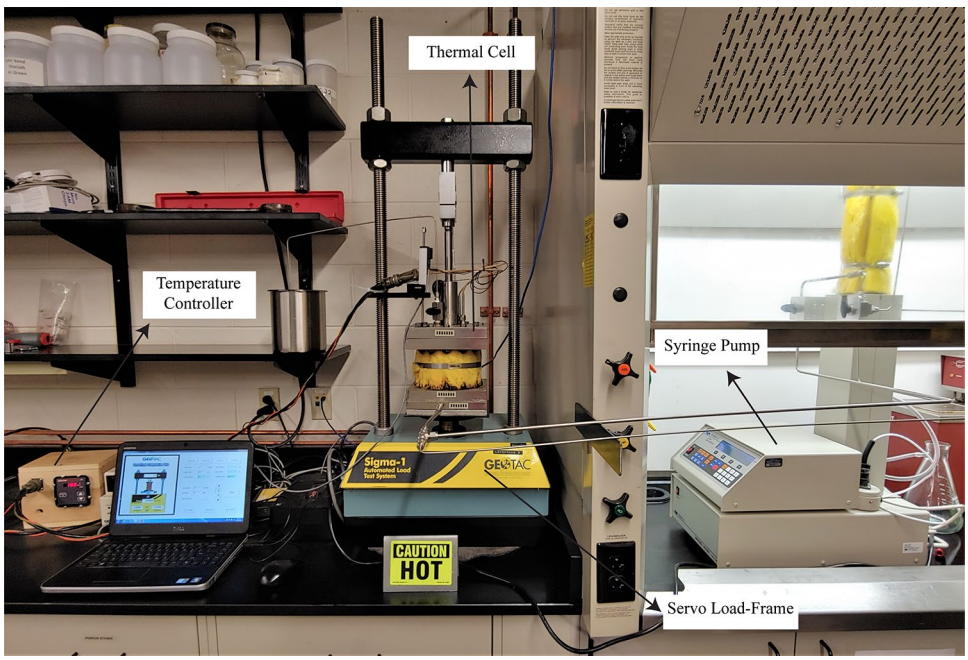

Fig. 5 The high-pressure thermal triaxial system

U-cup seal can seal the loading rod up to a pressure of 15 MPa at 150 °C. In addition, a 38.10 × 19.05 × 12.70 mm (1.5 × 0.75 × 0.5 in.) Buna-N cotton-reinforced piston-cup seal is placed around the loading rod beneath the top plate to help seal the loading rod (Fig. 1).

3 Specimen Preparation

3.1 Raw Material

The source rock salt used in preparing both synthetic

polycrystalline and natural single-crystal rock salt specimens was acquired from Windsor Salt Mine in Ontario, Canada. The $1.5 \times 1.5 \times 0.3$ m source rock salt was cut into smaller blocks with diligence to provide the raw material for preparing the specimens. Powder X-ray diffraction (PXRD) revealed that the material is 99.9% NaCl.

3.2 Polycrystalline Rock Salt Specimens

Crushed Rock salt grains with a size smaller than 0.075 mm (US sieve #200) were used to prepare the polycrystalline specimens. Three types of polycrystalline halite specimens were synthesized to represent various polycrystalline rock salt formations. The synthesis procedures of the polycrystalline halite specimens are not reported in this paper for the sake of brevity and the reader is referred to Moslehy and Alshibli (2021) for more details. Dry polycrystalline halite specimens were made by cold-pressing halite grains (containing 0.1% moisture) in three layers with equal thicknesses at 200 MPa uniaxial stress. Dry specimens were fine-grained with an average grain size of 0.15 μm and possessed a global porosity of about 7.2%. Porosity and average grain size inside dry specimens at the top layer were 5.8% and 0.13 μm, respectively. Porosity and average grain size of dry specimens increased from the top layer to the bottom layer, where the porosity and average grain size were 8.1% and 0.18 μm, respectively. Dry specimens represent the younger polycrystalline rock salt formations that did not have the same amount of time for annealing when compared to older formations.

Dry-annealed polycrystalline halite specimens were prepared similar to the dry specimens; however, they were annealed at a temperature of 200 °C for 7 days after compaction. Dry-annealed specimens had a larger average grain size (0.40 μm) and their global porosities were about 1.8%. The average grain size increased in dry-annealed specimens from the top layer (0.17 μm) to the bottom layer (0.78 μm). Porosity, on the other hand, was at the highest within the middle layer (3.1%) compared to the top layer at 1.9% and the bottom layer at 1.2%. Dry-annealed specimens represent older bedded polycrystalline rock salt formations, where the grains had more time to anneal. The bedding in the mentioned formations is caused by different layers of sedimentation throughout the history of the formation.

Wet-annealed polycrystalline halite specimens were prepared by cold-pressing a mixture of halite grains and salt-saturated deionized de-aired water with a ratio of 75–25%, respectively. The cold-press was completed in three equal layers at 200 MPa uniaxial stress. Wet-annealed specimens were annealed at a temperature of 200 °C for 7 days as well and have an average grain size of 0.63 μm which is larger than the other two types. Wet-annealed specimens also had smaller global porosities compared to the other two types (0.8%). The average grain size and porosity of wet-annealed specimens were almost uniform alongside their height. However, the middle layer had a slightly smaller average grain size (0.60 μm) compared to 0.67 and 0.63 μm at the top and bottom layers, respectively. The porosity of the middle layer (1.3%) was also slightly higher than the top layer (0.8%) and the bottom layer (0.6%). Although most of the water was ejected during the cold-press process, some water could be trapped in the middle layer that caused its porosity to be slightly higher than the other two layers and prevented the grains from annealing and growing in size (Moslehy and Alshibli 2021). Wet-annealed specimens mimic old polycrystalline rock salt formations without clear beddings that have a higher uniformity in their properties. 6 of each type of specimens were prepared to conduct unconfined compression experiments at various temperatures. Table 1 lists the height, diameter, mass, and porosity of the specimens. Although the successful reproducibility of the properties of the specimens produced in this paper is briefly summarized here, the readers are referred to Moslehy and Alshibli (2021) for the detailed reproducibility discussion. Figure 6a, b shows the boundaries of the compaction layers of a dry and a dry-annealed specimen, which caused the beddings within the specimens. However, no clear bedding could be seen within wet-annealed specimens (Fig. 6c).

3.3 Single-Crystal Rock Salt Specimens

Halite's face-centered-cubic (FCC) crystal structure with natural cleavage planes on {1 0 0} crystal planes makes preparing standard cylindrical rock cores quite futile. As a result, cuboidal-shaped specimens with an average height of ~ 45.00 mm and a height to width or length ratio of 2:1 were adopted in this study. The existence of visible orthogonal {1 0 0} cleavage planes within the nearly transparent source rock was used as an identifier for locating large single crystals within the source rock and their orientation. Large cubical single crystals with dimensions of ~ 76.20 mm were separated from the source rock. The crystal orientations of the single crystals were estimated to be aligned with the cube's surfaces. Specimens with three different crystal orientations were then cut from the single-crystal cubes with the following orientations: parallel to [1 0 0], 19° to (1 0 0) in (0 1 0), and 30° to (1 0 0) in (0 1 0). The crystal orientations of the specimens in the Bunge Euler definition were $\begin{bmatrix} \varphi_1 = 0 \\ \Phi = 0 \\ \varphi_2 = 0 \end{bmatrix}$, $\begin{bmatrix} \varphi_1 = 19^\circ \\ \Phi = 0 \\ \varphi_2 = 0 \end{bmatrix}$, and $\begin{bmatrix} \varphi_1 = 30^\circ \\ \Phi = 0 \\ \varphi_2 = 0 \end{bmatrix}$, respectively; therefore, for simplicity, these specimens are referred to as 0°, 19°, and 30° specimens, respectively. φ_1, Φ, and φ_2 in order are the

Table 1 Initial physical properties of polycrystalline rock salt specimens

Specimen	Type	Height (mm)	Diameter (mm)	Mass (g)	Porosity (%)
D_1	Dry	51.8	25.9	55.21	6.8
D_2		53.5	25.9	57.14	6.9
D_3		53.7	25.5	55.24	7.4
D_4		47.4	25.5	48.51	7.7
D_5		52.9	25.9	56.04	7.3
D_6		53.5	25.9	56.91	7.0
DA_1	Dry-annealed	50.0	25.4	54.03	1.6
DA_2		50.4	26.0	57.37	1.5
DA_3		47.5	25.6	52.16	2.1
DA_4		41.2	25.3	44.06	1.8
DA_5		45.6	25.3	48.91	2.0
DA_6		39.5	25.3	42.25	1.8
WA_1	Wet-annealed	40.5	25.5	44.46	0.7
WA_2		48.2	24.6	49.09	1.0
WA_3		46.3	25.5	50.67	0.8
WA_4		46.2	24.8	47.88	0.9
WA_5		48.4	25.5	53.21	0.8
WA_6		44.8	25.5	49.09	0.8

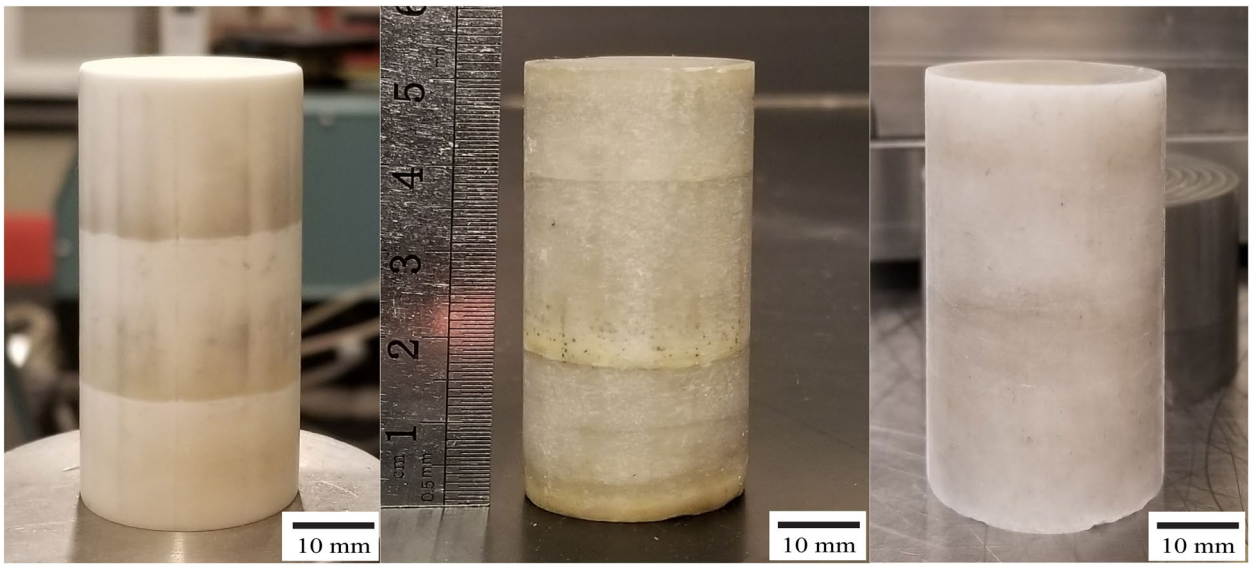

(a) Dry Specimen **(b)** Dry-annealed Specimen **(c)** Wet-annealed Specimen

Fig. 6 Photos of polycrystalline rock salt specimens

counterclockwise rotation angles of the specimen's axes about the *z*-axis, [1 0 0] direction, and [0 0 1] direction, to transfer specimen axes to the crystal axes. Specimens were gradually sanded with P3000 sandpaper to fine-tune their crystal orientation and to smooth their surface. Figure 7 shows a representative specimen of each type. The crystal orientations of the specimens were verified by conducting Laue X-ray diffraction (LXRD) experiments on 6 representative specimens to determine their crystal orientations with respect to the specimens' surface. 6 specimens of each crystal orientation were prepared to conduct the unconfined compression experiments at various temperatures (Table 2).

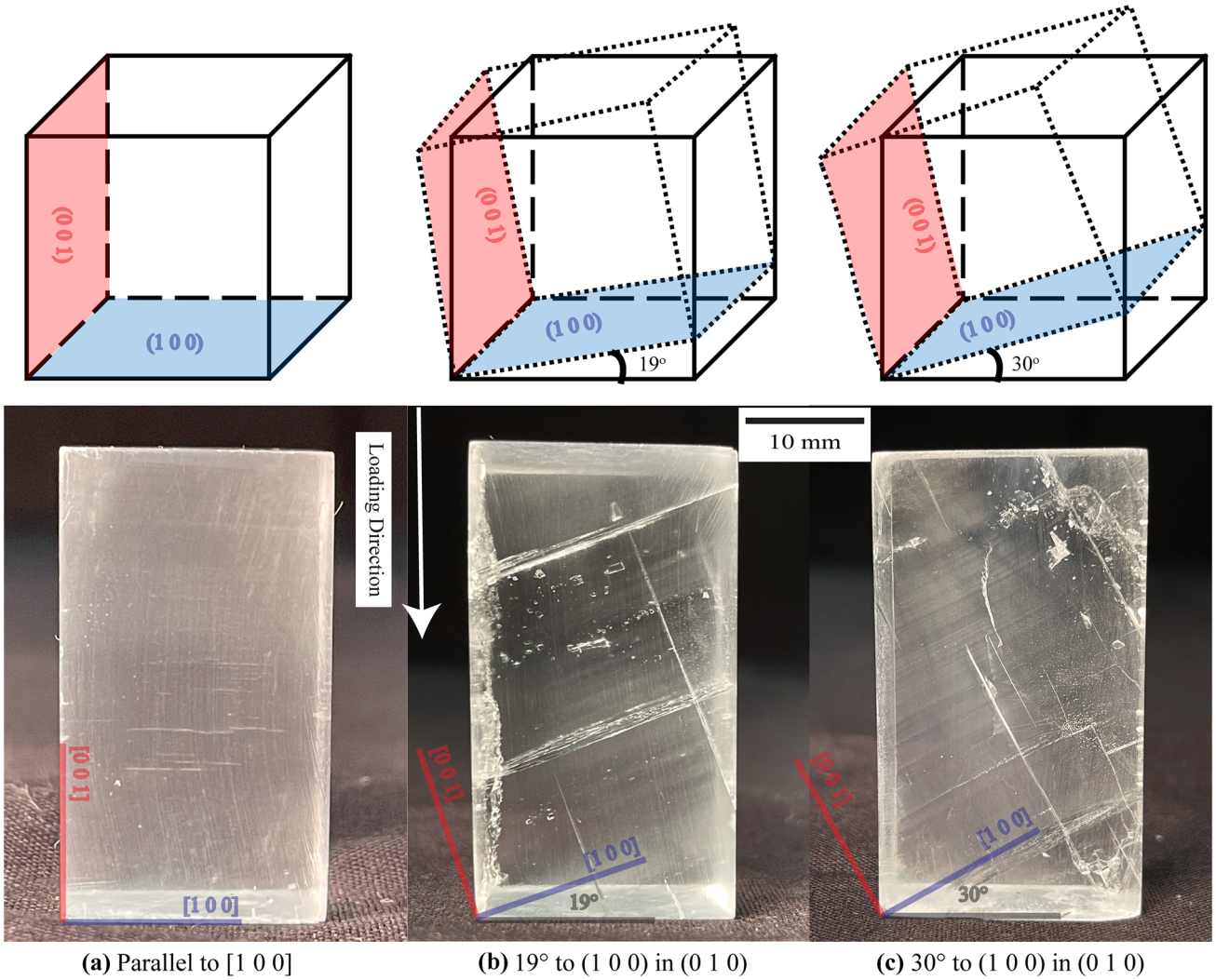

(a) Parallel to [1 0 0] **(b)** 19° to (1 0 0) in (0 1 0) **(c)** 30° to (1 0 0) in (0 1 0)

Fig. 7 Single-crystal rock salt specimens. The solid lines show the specimen's edges and the dotted lines show the specimen's crystal orientation

4 Unconfined Compression Experiments

4.1 Polycrystalline Specimens

Strain-controlled uniaxial compression experiments were conducted on 18 specimens employing the new high-pressure thermal cell. The experiments were carried out at 20°, 100°, and 150 °C, and two specimens of each polycrystalline rock salt type were tested at each temperature. The experiments were performed according to ASTM D7012 (2014) standard using a constant loading strain rate of $1.7 \times 10^{-4} s^{-1}$. The results are summarized in Table 3, and Fig. 8a, b, c shows the axial strain (ϵ_1) versus axial stress (σ_1) relationships of dry, dry-annealed, and wet-annealed specimens, respectively, at various temperatures. Dry specimens exhibited an average unconfined compressive strength (σ_u) of 64.38 MPa at room temperature (20 °C), which is much higher than dry-annealed and wet-annealed specimens' unconfined compressive strength at room temperature (39.58 and 41.02 MPa, respectively; Fig. 8). Bourcier et al. (2013) similarly found that polycrystalline rock salt specimens with smaller average grain sizes displayed a higher unconfined compressive strength. A smaller average grain size prevents the formation of connected crystal dislocations. On the other hand, dry specimens had high porosity grain boundaries, which are naturally immobile at room temperature (Guillope and Poirier 1979). The immobility of grain boundaries resulted in a surge in the unconfined compressive strength of the material and reduced its ductility, which explains the lesser ductility of dry specimens, ~2.84% axial strain at failure, compared to the other specimens (Fig. 8).

As mentioned earlier, dry-annealed specimens displayed a similar unconfined compressive strength to wet-annealed specimens at room temperature (Fig. 8b, c). This similarity is due to the comparably large average grain size of the dry-annealed and wet-annealed specimens, which

Table 2 Initial physical properties of single-crystal rock salt specimens

Specimen	Crystal orientation	Height (mm)	Length (mm)	Width (mm)	Mass (g)	Porosity (%)
0°_1_20 °C	Parallel to [1 0 0]	32.0	16.9	14.8	17.28	0.4
0°_2_20 °C		37.3	21.7	19.0	32.95	0.9
0°_3_100 °C		41.5	19.2	16.6	28.47	0.8
0°_4_100 °C		45.5	22.7	19.8	43.85	1.3
0°_5_150 °C		42.3	24.7	24.2	54.52	0.7
0°_6_150 °C		41.7	22.1	20.2	39.88	1.0
19°_1_20 °C	19° to (1 0 0) in (0 1 0)	49.1	32.7	27.5	95.3	0.6
19°_2_20 °C		37.2	24.2	22.3	42.88	1.7
19°_3_100 °C		46.3	30.2	26.3	79.15	0.9
19°_4_100 °C		49.6	26.4	19.0	53.61	0.7
19°_5_150 °C		38.1	26.3	23.3	49.97	1.5
19°_6_150 °C		38.7	24.7	21.6	43.77	2.3
30°_1_20 °C	30° to (1 0 0) in (0 1 0)	43.6	25.7	24.2	58.21	0.8
30°_2_20 °C		36.8	25.0	24.8	48.66	1.3
30°_3_100 °C		61.3	27.0	24.8	88.48	0.8
30°_4_100 °C		55.5	27.9	22.9	76.21	1.0
30°_5_150 °C		41.1	25.6	22.6	50.60	2.1
30°_6_150 °C		42.2	25.7	21.5	49.50	2.3

Table 3 Summary of unconfined compression experiment results on the three types of polycrystalline rock salt specimens at various temperatures

Specimen	Temperature (°C)	Yield stress (MPa)	Unconfined compressive strength (MPa)	Axial strain at failure (%)	Elastic modulus (GPa)
D_1	20	64.37	66.83	2.90	2.6
D_2		56.34	61.92	2.78	2.6
D_3	100	54.52	55.90	3.21	2.5
D_4		55.51	57.85	3.40	2.5
D_5	150	35.07	43.78	7.83	2.1
D_6		28.28	42.25	9.57	2.1
DA_1	20	18.69	40.19	4.01	2.4
DA_2		18.69	38.96	3.45	2.4
DA_3	100	16.48	35.19	9.53	1.4
DA_4		16.43	34.12	7.18	1.4
DA_5	150	16.09	30.56	10.10	0.7
DA_6		15.62	30.99	11.05	0.7
WA_1	20	12.79	39.87	7.97	3.6
WA_2		13.27	42.17	7.78	2.4
WA_3	100	13.27	36.98	16.26	1.4
WA_4		11.07	34.47	12.04	1.4
WA_5	150	12.72	29.71	17.89	1.4
WA_6		13.22	31.92	20.90	1.1

allowed crystal dislocations to form and grow. However, the dry-annealed specimens' ductility, ~ 3.73% axial strain at failure, was considerably less than wet-annealed specimens' ~ 7.88% axial strain at failure (Fig. 8b, c). The beddings within dry and dry-annealed specimens in addition to their high porosity grain boundaries could further obstruct crystal dislocations in comparison to wet-annealed specimens (Schenk et al. 2006). Moreover, the presence of water within grain boundaries of wet-annealed specimens facilitated the grain boundary migration. Comparing the results of unconfined compression experiments on the three types of polycrystalline specimens at various temperatures, the

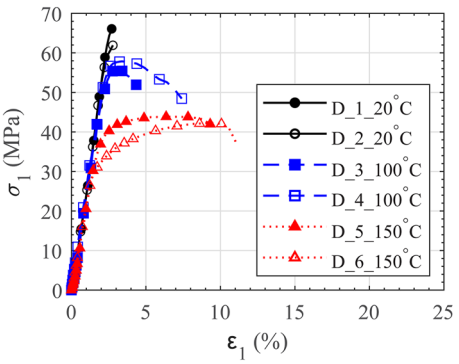

(a) Dry Specimens

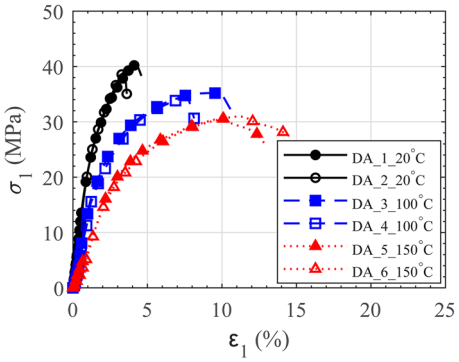

(b) Dry-annealed Specimens

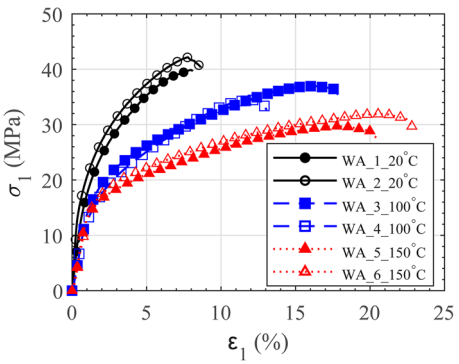

(c) Wet-annealed Specimens

Fig. 8 Axial strain versus axial stress during unconfined compression experiments on polycrystalline specimens at various temperatures

trend is the same in the results of different polycrystalline specimens: the increase of temperature leads to a decline of the unconfined compressive strength and gain of ductility (Fig. 8). During the compression experiments at elevated temperatures, dynamic recrystallization of rock salt grains occurs (Watanabe and Peach 2002). Dynamic recrystallization increases the average grain size and eases the grain boundary migration, which were the causes of unconfined compressive strength drops and ductility gains.

The dry specimens tested at 150 °C showed work hardening and reached a steady-state flow stress during the tests due to grain boundary migration compared to the dry specimens tested at 20 °C and 100 °C. Moreover, the unconfined compressive strength dropped 33% at 150 °C compared to the unconfined compressive strength at room temperature. Dry grain boundary migration does not occur in polycrystalline rock salt at temperatures below 400 °C (Guillope and Poirier 1979); however, Schenk et al. (2006) showed a small presence of water (even 0.1%) at the grain boundaries allows grain boundary migration to occur at a temperature above 125 °C. Dry-annealed and wet-annealed specimens displayed work hardening and reached a steady-state flow stress during the experiments conducted above 100 °C due to the higher mobility of the grain boundaries caused by annealing. The unconfined compressive strength of dry-annealed and wet-annealed specimens decreased 25% from room temperature to 150 °C, in comparison to a 33% drop observed for dry specimens. Dry-annealed and wet-annealed specimens had experienced static recrystallization during their annealing; therefore, their unconfined compressive strengths showed less reduction. Moreover, wet-annealed specimens showed more increase in ductility at elevated temperatures in comparison to dry-annealed specimens due to the higher mobility of wet grain boundaries (Fig. 8).

4.2 Single-Crystal Specimens

Similar to the polycrystalline specimen experiments, a total of 18 single-crystal specimens (6 of each crystal orientation) were tested at the following condition: a pair of specimens with a specific crystal orientation at 20°, 100°, and 150 °C. The same constant loading strain rate of $1.7 \times 10^{-4} s^{-1}$ was used for testing the single-crystal specimens. Table 4 summarizes the results of the experiments, and Fig. 9a, b, c depicts the axial strain (ϵ_1) versus σ_1 relationships of 0°, 19°, and 30° specimens, respectively, at various temperatures.

Fracture (failure) of FCC single crystals (Fig. 10a) is often controlled by the activation of either some slip systems or cleavage planes within the crystal (Cox Jr 1954). Slip systems are plastic deformation mechanisms causing the crystal to fail in a ductile manner, while the activation of cleavage planes causes a brittle fracture of the crystal (Aoki and Izumi 1979; Wimmer et al. 1963). Rock salt has 6 primary slips systems along {1 1 0} planes on < 1 − 1 0 > directions (Fig. 10b). They are accompanied by 6 secondary slip systems along {1 0 0} planes on < 0 1 1 > directions (Fig. 10c) and 12 more secondary slip system along {1 1 1} planes on < 1 − 1 0 > directions (Fig. 10d). Any of these 24 slip systems activates if the resolved shear stress (RSS) on the slip system exceeds the critical resolved shear stress (CRSS) of the slip system. RSS on any slip system can be calculated using Eq. (1). Rock salt's orthogonal cleavage planes are along {1 0 0} planes, where the activation of a cleavage plane depends on the cleavage plane's resolved normal stress

Table 4 Summary of unconfined compression experiment results on single-crystal rock salt specimens with different crystal orientations at various temperatures

Specimen	Temperature (°C)	Yield stress (MPa)	Unconfined compressive strength (MPa)	Axial strain at failure (%)	Elastic modulus (GPa)
0°_1_20 °C	20	8.06	19.68	8.77	0.9
0°_2_20 °C		8.66	19.76	7.77	0.9
0°_3_100 °C	100	7.54	18.92	12.74	0.7
0°_4_100 °C		8.03	18.86	15.02	1.0
0°_5_150 °C	150	5.79	19.05	20.69	0.5
0°_6_150 °C		6.62	17.69	21.24	1.0
19°_1_20 °C	20	7.46	21.41	8.45	1.1
19°_2_20 °C		9.58	22.36	8.55	2.0
19°_3_100 °C	100	10.72	22.48	12.68	0.7
19°_4_100 °C		7.38	21.91	13.35	0.7
19°_5_150 °C	150	6.86	22.79	22.81	0.5
19°_6_150 °C		7.48	22.29	20.07	0.7
30°_1_20 °C	20	12.47	38.48	8.01	2.0
30°_2_20 °C		12.08	37.88	8.90	2.0
30°_3_100 °C	100	12.62	30.25	8.79	1.1
30°_4_100 °C		11.37	29.29	7.81	1.1
30°_5_150 °C	150	10.09	22.72	15.66	1.3
30°_6_150 °C		9.81	24.07	17.86	0.9

(RNS) surpassing the plane's critical resolved normal stress (CRNS). RNS on a cleavage plane is calculated from Eq. (2):

$$\mathrm{RSS} = \cos\left(\emptyset\right) \times \cos\left(\lambda\right) \times \sigma = m \times \sigma \tag{1}$$

$$\mathrm{RNS} = \cos^2\left(\emptyset\right) \times \sigma = \text{cleavage factor} \times \sigma \tag{2}$$

where ∅ is the angle between the cleavage or slip plane and the stress axis, λ is the angle between the slip direction and the stress direction, σ is the applied stress, and m is the slip system's Schmid factor. Table 5 shows the Schmid and cleavage factors of the specimens with different crystal orientations. The CRSS values of rock salt's primary slip systems are generally smaller than the secondary slip systems' CRSS (Carter and Heard 1970); therefore, normally rock salt's primary slip systems are more active during single-crystal rock salt deformation (depending on the loading direction). However, the secondary slip systems' CRSS values are more sensitive to an increase of temperature; therefore, at elevated temperatures, the secondary slip systems may become activated more often. Smaller applied strain rates can also facilitate the activation of rock salt's slip systems resulting in a ductile creep rupture of the specimens, which prevails the more brittle cleavage fracture. The cleavage fracture of rock salt is a function of the density of the ionic bonds at cleavage planes. Rock salt single crystals with more defects and atomic vacancies naturally have a lower ionic bond density at their cleavage planes yielding a lower CRNS value (Schultz et al. 1994).

Figure 11a shows the results of a representative specimen of each crystal orientation tested at various temperatures. The specimens loaded parallel to [1 0 0] crystal planes (0° specimens) at 20 °C had a lower average unconfined compressive strength (19.72 MPa) in comparison to the specimens loaded on 19° to (1 0 0) in (0 1 0) and 30° to (1 0 0) in (0 1 0) with average unconfined compressive strengths of 22.39 MPa and 38.18 MPa, respectively. However, the unconfined compressive strength of the 0° specimens was lower than the confined extensional strength of similar specimens (28 MPa) reported by Carter and Heard (1970). The specimens prepared by Carter and Heard (1970) were synthetic specimens that normally contain fewer artifacts, impurities, and inclusions when compared to the naturally sourced specimens tested in this study. Figure 12a, d shows specimen 0°_1_20 °C before and after the test, respectively. The macroscopic observations of 0° specimens after the failure manifest the distortion of the {1 0 0} cleavage planes on the {1 1 0} < 1 − 1 0 > slip system and activation of a significant number of the {1 0 0} cleavage planes, meaning cleavage fracture had eventually governed the failure. Single-crystal rock salt (based on tests conducted on synthetic rock salt) is normally expected to undergo a significant continuous dislocation on an activated slip system at room temperature until the specimen is deemed failed because of the amount of the axial strain or the specimen fractures due to lattice rotations caused by the accumulated plastic deformation on the slip systems. However, as shown here, the defects and

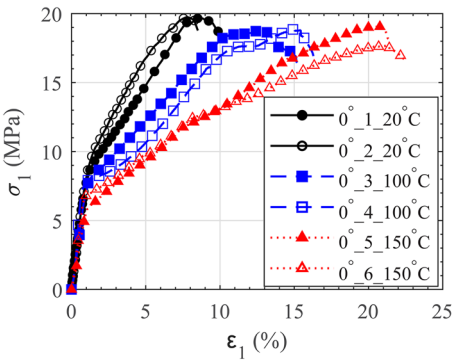

(a) Parallel to [1 0 0]

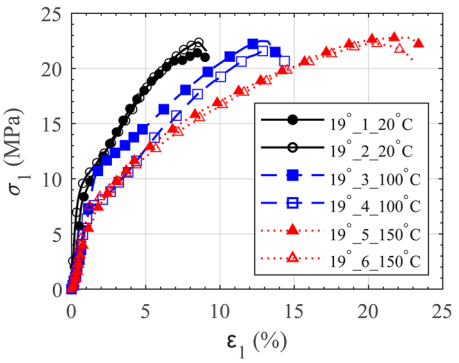

(b) 19° to (1 0 0) in (0 1 0)

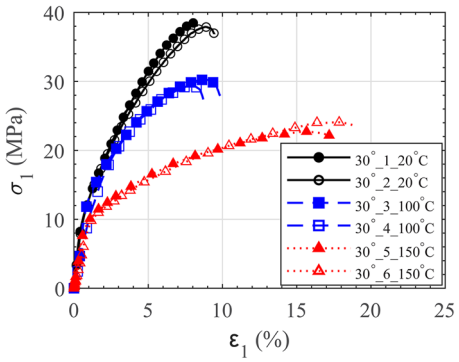

(c) 30° to (1 0 0) in (0 1 0)

Fig. 9 Axial strain versus axial stress during unconfined compression experiments on single-crystal specimens with different crystal orientations at various temperatures

flaws within natural rock salt single crystals can facilitate a cleavage fracture to occur much sooner than the axial strains reach the expected values. The 0° specimens also possessed an average elastic modulus of 0.9 GPa compared to 1.5 and 2.0 GPa for the 19° and 30° specimens, which was also lower than the 1.76 GPa reported by Carter and Heard (1970) for synthetic 0° specimens.

The specimens loaded on 19° to (1 0 0) in (0 1 0) at 20° C showed an average unconfined compressive strength of 21.89 MPa. The unconfined compressive strength of 19° specimens is interestingly $\frac{1}{19°\text{cleavage factor}}$ times higher than the unconfined compressive strength of 0° specimens. 19° specimens also exhibited the same distortion and significant activation of the {1 0 0} cleavage planes (Fig. 12b, e). The conjunction of these two observations means that the dominant accumulated slip system during the tests on 19° specimens had been {1 1 0}<1 − 1 0> and they failed by cleavage fracture on the {1 0 0} planes. The 38.18 MPa average unconfined compressive strength of 30° specimens, on the other hand, does not follow a similar relationship with the 0° specimens. Visual inspection of 30° specimens tested at 20 °C (Fig. 12c, f) did not reveal a significant amount of distortion of the {1 0 0} planes along the {1 1 0}<1 − 1 0> slip system. One explanation could be activation of some of the {1 1 1}<1 − 1 0> slip systems which had an increased Schmid factor of 1.18 on this specific crystal orientation. The dislocations caused by slipping on the {1 1 1}<1 − 1 0> slip system due to their directions can impede the propagation of the {1 0 0} cleavage planes making the specimens fracture at a higher σ_1 under the same applied ϵ_1.

Figure 11b shows the changes in the unconfined compressive strength of the specimens with an increase in temperature, where the unconfined compressive strength of 0° and 19° specimens did not change with the increase of temperature from 20 to 150 °C, while 30° specimens and all polycrystalline specimens showed a decrease in their unconfined compressive strength. Increasing the temperature not only can reduce the value of CRSS and CRNS on slip systems and cleavage planes but also can cause a change in the most active slip system at any time during the test and eventually the failure mode. 0° and 19° specimens' yield stress and the work-hardening rate decreased at higher temperatures in addition to the fact that their unconfined compressive strength did not change (Fig. 9a, b). This observation provides clear evidence that the {1 1 0}<1 − 1 0> still had been the dominant accumulated slip system, while its CRSS value had been decreased and the dislocation on the {1 1 0}<1 − 1 0> slip system was facilitated at elevated temperatures. Moreover, the value of CRNS for 0° and 19° specimens did not change and the specimens eventually after showing a significant amount of axial strain (>20%) fractured by the activation of the {1 0 0} cleavage planes. The unconfined compressive strength of the 30° specimens showed a significant drop at elevated temperatures. At 100 °C, 30° specimens did not show any drop in their yield strength and their ductility was still comparable to the specimens tested at 20 °C. However, the increase of temperature to 150 °C resulted in a decrease in the yield strength of the 30° specimens, a significant decrease in the work-hardening rate, and a significant increase in their ductility. All of the aforementioned observations demonstrated a change in the complex interaction of the active slip systems within the specimen. Cater and Heard (1970) showed that CRSS value of the {1 0 0}<0 1 1> slip system decreases at a higher rate

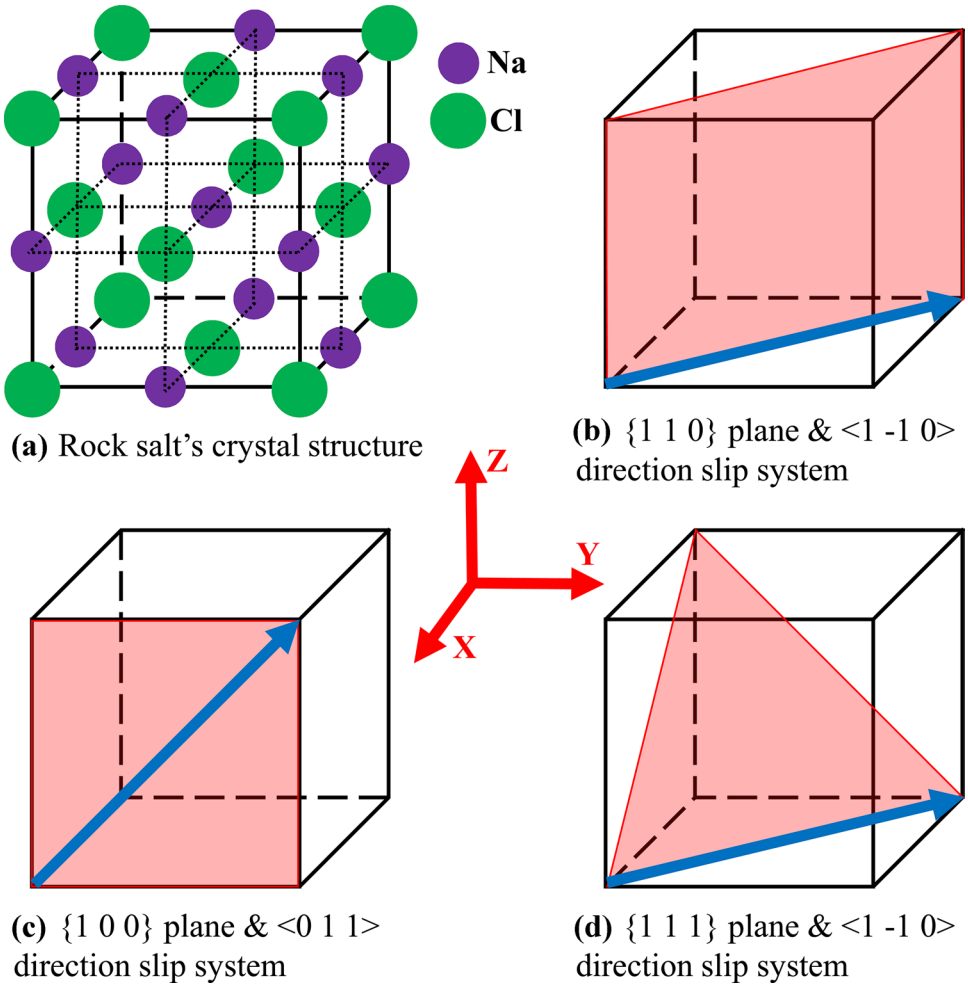

Fig. 10 Crystal structure of rock salt and its slip systems

Table 5 Schmid and cleavage factors of single-crystal specimens with different crystal orientations

Specimen	{1 1 0} < 1 − 1 0 >	{1 0 0} < 0 1 1 >	{1 1 1} < 1 − 1 0 >	{1 0 0} Cleavage
0°	1	0	1	1
19°	0.89	0.31	1.20	0.89
30°	0.75	0.43	1.18	0.75

compared to the other two slip systems, where at elevated temperatures CRSS of the {1 0 0} < 0 1 1 > slip system can even become smaller than CRSS of the {1 1 1} < 1 − 1 0 > slip system. The plastic deformations on the {1 0 0} < 0 1 1 > slip system are along the {1 0 0} cleavage planes; therefore, if activated, they facilitate the propagation of the {1 0 0} cleavage planes (in contrast to the plastic deformations on the {1 1 1} < 1 − 1 0 > slip system). At 150 °C, the unconfined compressive strength of the 30° specimens is $\frac{1}{30°\text{cleavage factor}}$ times of the unconfined compressive strength of 0° specimens at 150 °C. This observation shows that at least some {1 0 0} < 0 1 1 > slip systems had been activated during the tests conducted at 150 °C on 30 specimens.

5 Conclusions

In this paper, a new high-pressure thermal triaxial cell was designed whose features made it a suitable and safe apparatus for testing rock salt. The thermal cell is cost-effective considering its application and is easy to fabricate. It is capable of reaching a maximum confining pressure of 15 MPa (a PTFE spring-loaded U-cup seal substitution needed for confining pressures higher than 6.9 MPa), a maximum working temperature of 150 °C, a maximum 1.7 °C heat gradient alongside the height of the cell, and a maximum of 44.5 kN axial load.

Three different types of polycrystalline rock salt specimens were prepared in this study to investigate the influence of temperature on the strength properties of polycrystalline rock salts with different grain sizes and grain boundary properties. 18 unconfined compression experiments were then conducted on the specimens at various temperatures which

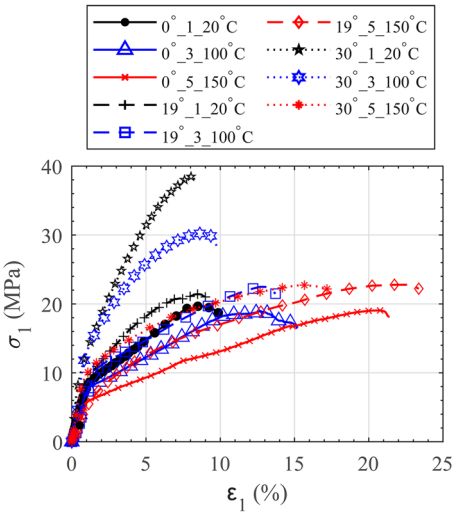

(a) Single crystal specimens with different orientations tested at various temperatures

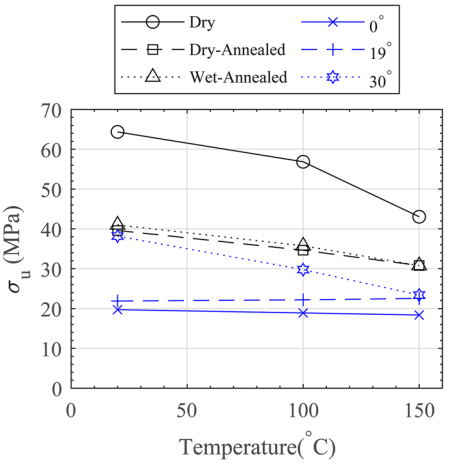

(b) Temperature's effect on unconfined compressive strength of the specimens

Fig. 11 Effect of temperature on the unconfined compressive of various rock salt specimens

lead to the following conclusions: (1) fine-grained rock salt containing nominally dry grain boundaries has the highest unconfined compressive strength and is the most brittle type of polycrystalline rock salt; (2) annealing regardless of the grain boundary water content results in a decrease in the unconfined compressive strength and increases the ductility; (3) bedding planes decrease rock salt's ductility; (4) increasing temperature in all cases decreases the unconfined compressive strength of polycrystalline rock salt and increases its ductility, where fine-grained rock salt with dry grain boundaries (younger rock salt formations) are more susceptible to the mentioned thermal changes.

Finally, natural single-crystal rock salt specimens with three different crystal orientations with respect to the loading direction were prepared for investigating the influence of crystal orientation and temperature on strength of natural single-crystal rock salt using the unconfined compression experiment. 18 tests were conducted at various temperatures which yielded the following conclusions: (1) natural single-crystal rock salt is more brittle and has a smaller unconfined compressive strength than synthetic single-crystal rock salt (typically tested in the literature; (2) cleavage fracture occurs at smaller applied axial strains in natural rock salt; (3) the loading direction with respect to rock salt's crystal orientation significantly influences its strength, where generally rotation of the loading direction from parallel to [1 0 0] direction to 30° to (1 0 0) in (0 1 0) direction increases the unconfined compressive strength; (4) elevation of temperature does not affect rock salt's response in all crystal orientations the same. Increasing the temperature resulted in a lower yield strength, a lower work-hardening rate, and a higher ductility rock salt tested parallel to [1 0 0] and 19° to (1 0 0) in (0 1 0). However, the ductility and yield strength of rock salt tested on 30° to (1 0 0) in (0 1 0) did not change before increasing the temperature to 150°.

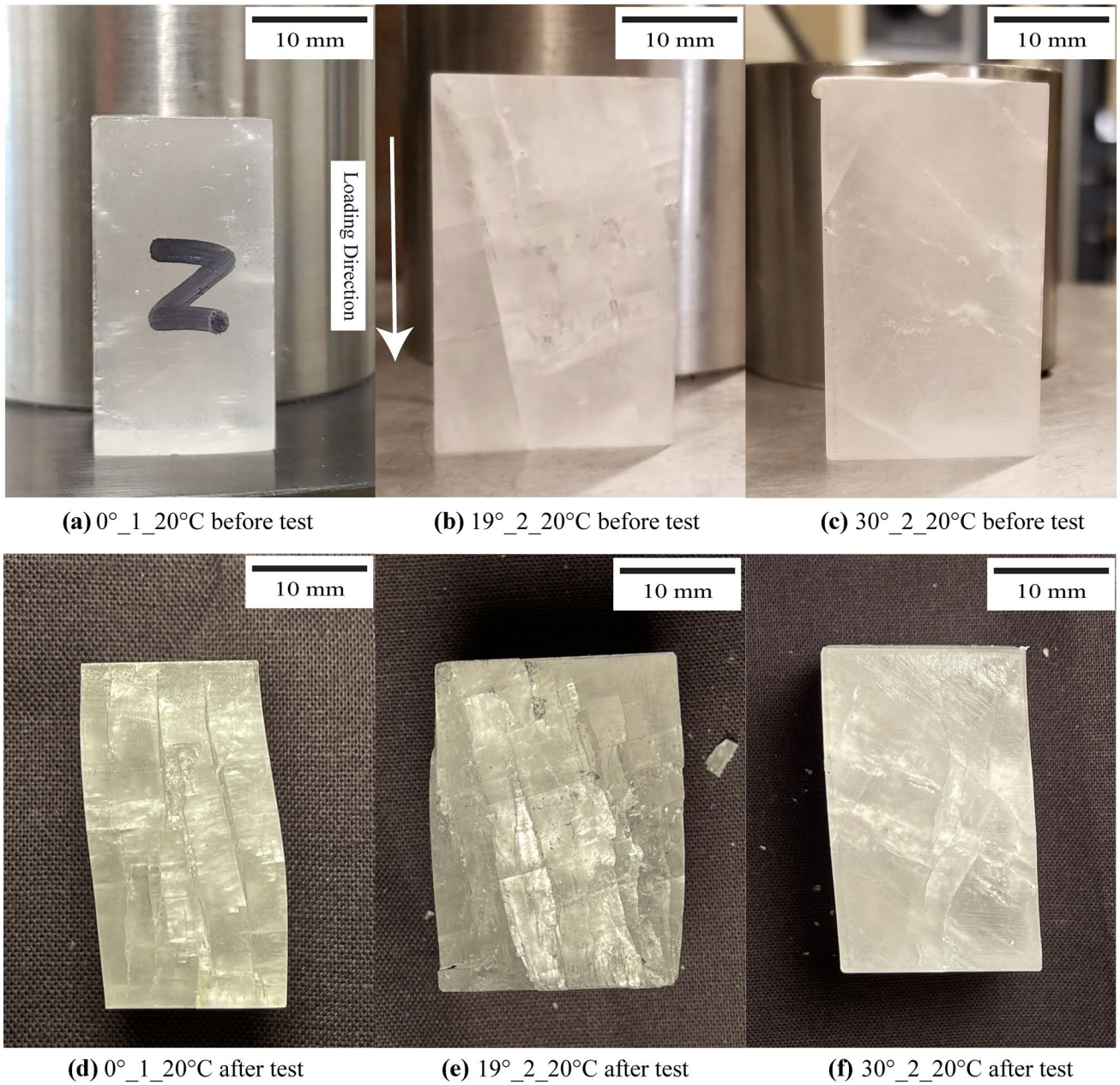

Fig. 12 Single-crystal specimens with different crystal orientations before and after unconfined compression tests

Acknowledgements This material is based on work supported by the National Science Foundation (NSF) under Grant # CMMI-1641054. Any opinions, findings, conclusions, and recommendations expressed in this material are those of the authors and do not necessarily reflect the views of NSF. PXRD and LXRD were acquired at the Joint Institute for Advanced Materials (JIAM) Diffraction Facility of the University of Tennessee, Knoxville. The authors are grateful to Tyler Galyon, Ibrahim Aklouk, Karen Abercrombie, and Jeremy Melton, undergraduate research assistants at the University of Tennessee, Knoxville, for their help in preparing some of the specimens.

Funding This material is based on work supported by the National Science Foundation under Grant No. CMMI-1641054.

Availability of Data and Materials Not applicable.

Code Availability Not applicable.

Declaration

Conflict of interest The authors declare that they have no conflict of interest.

References

Alshibli K, Jarrar ZA (2020) Four-dimensional dynamic synchrotron microcomputed tomography imaging of gas-water interface at high pressure and low temperature. Geotech Test J 44(4):1000–1014

Aoki K, Izumi O (1979) Cleavage fracture of the intermetallic compound Ni3Ge single crystals. Acta Metall 27(5):807–816

ASTM (2014) D7012-14 (2014) Standard test method for compressive strength and elastic moduli of intact rock core specimens under varying states of stress and temperatures. ASTM International, West Conshohocken. https://doi.org/10.1520/D7012-14E01

Bishop AW, Donald IB (1961) The experimental study of partly saturated soil in the triaxial apparatus. In: Proceedings of the 5th international conference on soil mechanics and foundation engineering, Paris, pp 13–21

Bishop AW, Wesley LD (1975) A hydraulic triaxial apparatus for controlled stress path testing. Geotechnique 25(4):657–670

Bourcier M, Bornert M, Dimanov A, Héripré E, Raphanel JL (2013) Multiscale experimental investigation of crystal plasticity and grain boundary sliding in synthetic halite using digital image correlation. J Geophys Res Solid Earth 118(2):511–526

Caballero JA, Conesa JA, Martín-Gullón I, Font R (2005) Kinetic study of the pyrolysis of neoprene. J Anal Appl Pyrol 74(1):231–237

Carter NL, Hansen FD (1983) Creep of rocksalt. Tectonophysics 92(4):275–333

Carter NL, Heard HC (1970) Temperature and rate dependent deformation of halite. Am J Sci 269(3):193–249

Cekerevac C, Laloui L, Vulliet L (2005) A novel triaxial apparatus for thermo-mechanical testing of soils. Geotech Test J 28(2):161–170

Cox JJ (1953) Critical stresses for slip, twinning, and cleavage in single crystals of iron. The Ship Structures Committee. No. SSC-66 Final Rpt. 1954

Davis KE, Guha TK, Henderson RL (1978) High temperature underground thermal energy storage. Thermal Energy Storage In. p 62

De Las Cuevas C, Pueyo JJ (1995) The influence of mineralogy and texture in the water content of rock salt formations. Its implication in radioactive waste disposal. Appl Geochem 10(3):317–327

Eastman (2020) Therminol 55 Heat Transfer Fluid. <https://www.therminol.com/product/71093433>. 11 May 2020

Evans AG, Gilling D, Davidge RW (1970) The temperature-dependence of the strength of polycrystalline MgO. J Mater Sci 5(3):187–197

Fredrich JT, Coblentz D, Fossum AF, Thorne BJ et al (2003) Stress perturbations adjacent to salt bodies in the deepwater Gulf of Mexico. In: SPE annual technical conference and exhibition

Ghembaza MS, Taibi S, Fleureau JM (2015) New thermal triaxial apparatus for unsaturated soils using the osmotic method. Arab J Geosci 8(6w):3365–3380

Guillope M, Poirier JP (1979) Dynamic recrystallization during creep of single-crystalline halite: an experimental study. J Geophys Res Solid Earth 84(B10):5557–5567

Hansen FD, Leigh CD (2011) Salt disposal of heat-generating nuclear waste. Sandia National Laboratories Albuquerque, NM

Jaradat KA, Abdelaziz SL (2020) Thermomechanical triaxial cell for rate-controlled heating-cooling cycles. Geotech Test J 43(4):1022–1036

Knudsen FP (1959) Dependence of mechanical strength of brittle polycrystalline specimens on porosity and grain size. J Am Ceram Soc 42(8):376–387

Lebensohn RA, Dawson PR, Kern HM, Wenk HR (2003) Heterogeneous deformation and texture development in halite polycrystals: comparison of different modeling approaches and experimental data. Tectonophysics 370(1–4):287–311

Liang WG, Xu SG, Zhao YS (2006) Experimental study of temperature effects on physical and mechanical characteristics of salt rock. Rock Mech Rock Eng 39(5):469–482

Locke CW, Severino A, Via FL, Reyes M, Register J, Saddow SE (2012) Chapter 2 - SiC films and coatings: amorphous, polycrystalline, and single crystal forms. In: Saddow SE (ed) Silicon carbide biotechnology. Elsevier, Oxford, pp 17–61

Marques FO, Burg J-P, Armann M, Martinho E (2013) Rheology of synthetic polycrystalline halite in torsion. Tectonophysics 583:124–130

Mishra DA, Janecek I (2017) Laboratory triaxial testing-from historical outlooks to technical aspects. ISRM European Rock Mechanics Symposium-EUROCK 2017, OnePetro

Moslehy A, Alshibli K (2021) Assessment of the properties of polycrystalline rock salt synthesized under nominally dry and wet conditions. J Rock Mech Geotech Eng 13(1):311–320

Mouritz AP (2012) 4 - Strengthening of metal alloys. In: Mouritz AP (ed) Introduction to aerospace materials. Woodhead Publishing, pp 57–90

Ostapenko NI, Sugakov VI, Shpak MT (1993) Dislocations and optical properties of organic crystals. In: Spectroscopy of defects in organic crystals. Springer Netherlands, Dordrecht, pp 133–158

Schenk O, Urai JL, Piazolo S (2006) Structure of grain boundaries in wet, synthetic polycrystalline, statically recrystallizing halite—evidence from cryo-SEM observations. Geofluids 6(1):93–104

Schultz RA, Jensen MC, Bradt RC (1994) Single crystal cleavage of brittle materials. Int J Fract 65(4):291–312

Sedlmayr A (2014) Experimental investigations of deformation pathways in nanowires. KIT Scientific Publishing

Senseny PE, Hansen FD, Russell JE, Carter NL, Handin JW (1992) Mechanical-behavior of rock salt—phenomenology and micromechanisms. Int J Rock Mech Min Sci 29(4):363–378

Takasugi T, Izumi O (1985) High temperature strength and ductility of polycrystalline Co3Ti. Acta Metall 33(1):39–48

Ter Heege JH, De Bresser JHP, Spiers CJ (2005) Dynamic recrystallization of wet synthetic polycrystalline halite: dependence of grain size distribution on flow stress, temperature and strain. Tectonophysics 396(1–2):35–57

Uchaipichat A, Khalili N, Zargarbashi S (2011) A temperature controlled triaxial apparatus for testing unsaturated soils. Geotech Test J 34(5):424–432

Watanabe T, Peach CJ (2002) Electrical impedance measurement of plastically deforming halite rocks at 125°C and 50 MPa. J Geophys Res Solid Earth 107(B1):ECV 2-1-ECV 2-12

Wawersik WR, Hannum DW (1980) Mechanical behavior of New Mexico rock salt in triaxial compression up to 200°C. J Geophys Res Solid Earth 85(B2):891–900

Wimmer FT, Kobes W, Fine ME (1963) Tensile properties of NaCl-BaNr solid solution single crystals. J Appl Phys 34(6):1775–1778

Xing W, Zhao J, Hou Z, Were P, Li M, Wang G (2015) Horizontal natural gas caverns in thin-bedded rock salt formations. Environ Earth Sci 73(11):6973–6985

Zhang S, Nakano H, Xiong Y, Nishimura T, Zhang F (2010) Temperature-controlled triaxial compression/creep test device for thermodynamic properties of soft sedimentary rock and corresponding theoretical prediction. J Rock Mech Geotech Eng 2(3):255–261

Publisher's Note Springer Nature remains neutral with regard to jurisdictional claims in published maps and institutional affiliations.